Tuning of Synaptic Integration in the Medial Entorhinal Cortex to the Organization of Grid Cell Firing Fields

Neuron
Article

Tuning of Synaptic Integration in the Medial Entorhinal Cortex to the Organization of Grid Cell Firing Fields

Derek L.F. Garden,[1,3] Paul D. Dodson,[1,3] Cian O'Donnell,[1,2] Melanie D. White,[1] and Matthew F. Nolan[1,*]
[1]Centre for Neuroscience Research and Centre for Integrative Physiology, R(D)SVS, University of Edinburgh, Hugh Robson Building, Edinburgh, EH8 9XD, Scotland, UK
[2]Neuroinformatics Doctoral Training Centre, Institute of Adaptive and Neural Computation, School of Informatics, University of Edinburgh, Edinburgh, EH8 9AB, Scotland, UK
[3]These authors contributed equally to this work
*Correspondence: mattnolan@ed.ac.uk
DOI 10.1016/j.neuron.2008.10.044

SUMMARY

Neurons important for cognitive function are often classified by their morphology and integrative properties. However, it is unclear if within a single class of neuron these properties tune synaptic responses to the salient features of the information that each neuron represents. We demonstrate that for stellate neurons in layer II of the medial entorhinal cortex, the waveform of postsynaptic potentials, the time window for detection of coincident inputs, and responsiveness to gamma frequency inputs follow a dorsal-ventral gradient similar to the topographical organization of grid-like spatial firing fields of neurons in this area. We provide evidence that these differences are due to a membrane conductance gradient mediated by HCN and leak potassium channels. These findings suggest key roles for synaptic integration in computations carried out within the medial entorhinal cortex and imply that tuning of neural information processing by membrane ion channels is important for normal cognitive function.

INTRODUCTION

A neuron's response to activation of a synaptic conductance is determined by its dendritic morphology, and by the identity and subcellular location of its membrane ion channels (Hausser et al., 2000; Magee, 2000; Williams and Stuart, 2003). These integrative properties are generally considered to be similar within a particular class of neuron and so are often used as identifiers to distinguish between neurons of different classes (Hattox and Nelson, 2007; Markram et al., 2004; McCormick et al., 1985; Spruston and Johnston, 1992; Sugino et al., 2006; Yuste, 2005). However, the distributed nature of cortical representations implies that different neurons within a particular class may receive or generate distinct signals, raising the question of whether the individual neurons of a particular class adapt their intrinsic integrative properties according to the precise form of the input signals they receive or to the exact nature of the computation they perform (Laughlin, 1981; Stemmler and Koch, 1999). In sensory and motor systems, where there is clear topographical organization of neural representations, a corresponding organization of ion channel expression and intrinsic excitability suggests that nonsynaptic integrative properties are optimized according to the specific features of the external environment that a particular neuron represents (Barnes-Davies et al., 2004; McLean et al., 2007; Reid et al., 2004). By contrast, computations underlying higher cognitive functions are usually modeled with networks of identical neurons (Hopfield, 1982; Wang, 2001), and little attention has been given to the possibility that in circuits that process polymodal information the rules that govern integration of synaptic inputs by each neuron may depend on the specific information that neuron represents.

Neurons in layer II of the medial entorhinal cortex (MEC) represent an animal's spatial location using topographically organized grid-like firing fields (Hafting et al., 2005). When an animal moves through its environment, the locations at which these neurons fire action potentials correspond to the apices of equilateral triangles ordered contiguously in a grid-like arrangement. Unlike neurons in sensory pathways, which encode a single sensory modality and form representations that are oriented to their sensory organ, superficial entorhinal neurons receive convergent polymodal inputs from the neocortex (Amaral and Witter, 1989) and encode representations that are oriented with respect to an animal's environment (Moser et al., 2008). The outputs from these superficial entorhinal neurons are a primary source of information used by the hippocampus for encoding and storage of episodic-like memories (Dolorfo and Amaral, 1998; Steffenach et al., 2005; van Groen et al., 2003; Witter et al., 2000). Recent studies demonstrate that the distance between the vertices of a neuron's grid field depends upon its location along the dorsal-ventral axis of the MEC. At the dorsal border of the MEC, neurons have firing fields that are separated by approximately 30 cm (Hafting et al., 2005). This spacing becomes progressively larger for neurons located more ventrally, and is several meters for some neurons in the ventral MEC (Brun et al., 2008; Fyhn et al., 2008). The cellular mechanisms that underlie the formation of grid fields or that determine their spacing are not at all clear. Several distinct models have been proposed (Moser

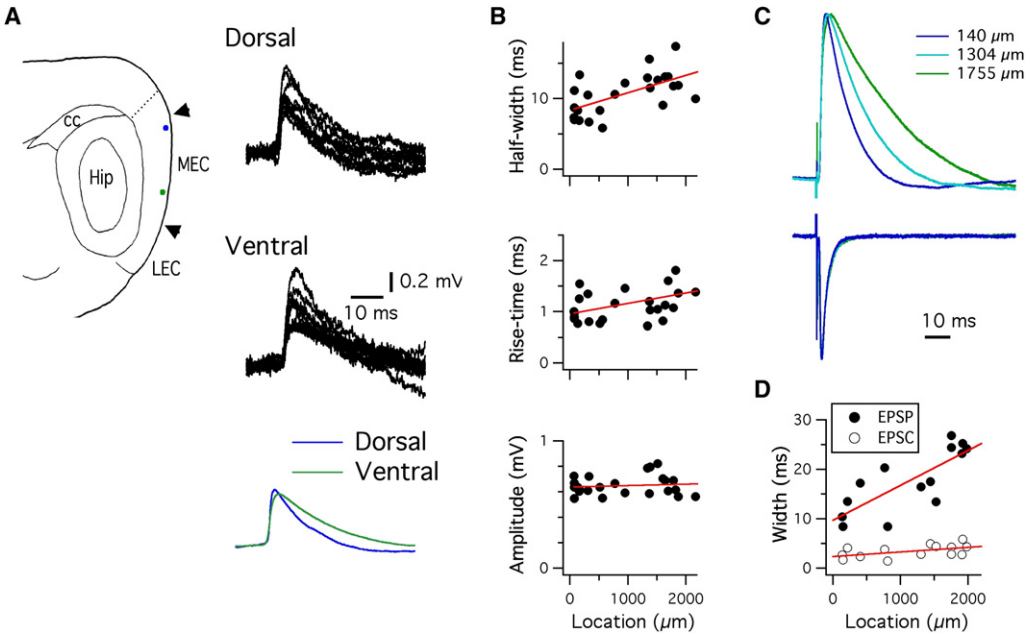

Figure 1. EPSP Waveform Varies as a Function of Location along the Dorsal-Ventral Axis of the MEC

(A) Examples of ten consecutive spontaneous EPSPs recorded from a stellate neuron in the dorsal MEC (upper right, location 136 μm) and a stellate neuron in the ventral MEC (middle right, location 1697 μm). Overlay of the average of >100 spontaneous EPSPs recorded from the dorsal cell (blue) and the ventral cell (green) (lower right). The schematic parasagittal brain section (left) illustrates the approximate location of the example neurons (blue and green filled circles), the border of the postrhinal and sensory cortices (dashed line), the dorsal and ventral borders of the MEC (arrow heads), hippocampus (Hip), corpus callosum (cc), and lateral entorhinal cortex (LEC).

(B) The median values for half-width (top), 20%–80% rise time (middle), and EPSP amplitude (bottom) are plotted as a function of location.

(C) Examples of normalized evoked EPSPs (top) and corresponding EPSCs (bottom) recorded from stellate neurons at three different locations along the dorsal-ventral axis of the MEC.

(D) EPSP (R^2 = 0.58, p = 0.0009) and EPSC (R^2 = 0.21, p = 0.055) half-width plotted as a function of location. Voltage- and current-clamp data are for responses to the same sets of synaptic inputs. Half-width data as a function of location are best fit with a linear model that accounts for whether measurements are from current- or voltage-clamp recordings (General Linear Test, p << 1e−6) and direct comparisons indicate that EPSC half-widths are significantly shorter than EPSP half-widths (Wilcox test, p < 1e−6).

et al., 2008), and there is experimental data to support both single-cell models (Giocomo et al., 2007) and recurrent-network models (Kumar et al., 2007). The kinetics of Hyperpolarization-activated Cyclic Nucleotide-gated (HCN) channels expressed by stellate neurons have been suggested to correlate with the dorsal-ventral organization of grid fields (Giocomo and Hasselmo, 2008). This may support a corresponding organization of oscillatory membrane activity recorded from stellate neurons (Giocomo et al., 2007). However, very little is known about the rules whereby neurons in the MEC transform their synaptic inputs into patterns of output, or about whether this transformation differs according to the properties of grid fields at a particular location along the dorsal-ventral axis of the MEC.

We have taken advantage of the anatomical organization of grid field representations within the MEC to directly address the organization of synaptic integration by stellate neurons and thereby explore the possibility that neurons that mediate higher cognitive processes integrate incoming synaptic activity according to the representations they encode. We show that integration of synaptic inputs varies as a function of a neuron's location along the dorsal-ventral axis of the MEC and provide evidence that this variation is accounted for by complementary gradients in a hyperpolarization-activated conductance and a leak K^+ conductance.

RESULTS

Synaptic Integration within the MEC Is Organized along a Dorsal-Ventral Gradient

We developed a parasagittal brain slice preparation to enable recordings at well-defined locations along the full extent of the dorsal-ventral axis of the MEC from adult mice (see Experimental Procedures). The major glutamatergic projection neurons within layer II of the MEC are stellate neurons (Alonso and Klink, 1993; Buckmaster et al., 2004; Klink and Alonso, 1997), which in this preparation demonstrated characteristic electrophysiological and morphological properties reported in previous studies (Figures 4, 5, and S1 available online) (Alonso and Klink, 1993). We evaluated spontaneous non-NMDA-glutamate-receptor-mediated excitatory postsynaptic potentials (EPSPs) recorded from stellate neurons (Figure 1A). Consistent with our hypothesis that synaptic responses may be tuned to the spatial resolution of grid fields, we found a striking increase in the rise time (R^2 = 0.19, p = 0.017) and half-width (R^2 = 0.37, p = 7.8e−4) of spontaneous EPSPs with increasing distance of stellate neurons from the dorsal pole of the MEC (Figure 1B). The amplitude of spontaneous EPSPs did not appear to depend on location (R^2 = −0.04, p = 0.76) (Figure 1B).

The waveform of synaptic potentials can be determined by the time course of the opening of postsynaptic receptors and by nonsynaptic neuronal integrative properties (Jack et al., 1975; Koch, 1999). To substantially influence the duration of an EPSP, the kinetics of the synaptic current must be similar to or slower than the postsynaptic membrane time constant (Rall, 1960). In this case the recorded excitatory postsynaptic currents (EPSCs) and EPSPs will have similar kinetics. To investigate this possibility we recorded EPSPs and corresponding EPSCs evoked by electrical stimulation of layer I (see Experimental Procedures). Consistent with our observations of spontaneous EPSPs, we found a gradient in the half-width of evoked EPSPs ($p = 0.0009$) (Figures 1C and 1D). However, while the half-width of EPSPs recorded from stellate neurons ranged from 8.4 to 26.9 ms, the time course of the corresponding voltage-clamped EPSCs was several-fold faster ($p < 1e{-}6$), with half-widths that ranged from 1.5 to 5.9 ms and that did not vary significantly as a function of location (Figures 1C and 1D). While a somatic electrode does not perfectly control the voltage at distal synapses, an imperfect voltage-clamp will cause somatically recorded EPSCs to have slower kinetics than the underlying synaptic current (Hausser and Roth, 1997; Williams and Mitchell, 2008), and therefore the difference between the kinetics of the somatically recorded EPSP and the underlying EPSC may be even larger than our estimates suggest. These observations also argue against the possibility that in neurons at different dorsal-ventral locations, the recorded synaptic potentials happen to arise at different dendritic locations, as in this case systematic differences in the voltage clamp would cause the waveform of EPSCs to show a similar location dependence to the EPSPs (Hausser and Roth, 1997; Williams and Mitchell, 2008). Thus, differences in synaptic properties, such as receptor composition or time course of glutamate in the synaptic cleft, are unlikely to account for the dorsal-ventral gradient in the waveform of EPSPs.

Does the variation in the waveform of EPSPs lead to differences in the temporal integration of synaptic inputs? By varying the interval between stimulation of two independent inputs, we determined the time window during which the earlier synaptic response could increase the peak depolarization obtained during the later synaptic response (Figure 2). The time window for integration of the two responses was narrowest in dorsal neurons (Figures 2A and 2C), increases steeply with distance from the dorsal border of the MEC, and is approximately three times wider in the most ventral cells compared with the most dorsal cells (slope = 12.9 ms mm^{-1}, $R^2 = 0.9$, $p = 0.0002$) (Figures 2B, 2D, and 2E). The half-duration of EPSPs evoked by both inputs again increased with distance of the recorded cell from the dorsal border of the MEC (dorsal input: $R^2 = 0.73$, $p = 0.004$; ventral input: $R^2 = 0.89$, $p = 0.0003$) (Figure 2F), whereas the amplitude and rise time of the evoked EPSPs did not demonstrate a significant dependence on location ($p > 0.4$) (Figures 2G and 2H). Thus, the time window for detection of coincident inputs by a stellate neuron varies as a function of location along the dorsal-ventral axis of the MEC.

While coincidence detection may be important for neural computations that rely on spike timing, other neural computations may instead rely on temporal summation of trains of input. Recordings from layer II of the MEC in freely behaving animals indicate that periods of gamma frequency (40–80 Hz) synaptic activity occur nested within theta frequency (5–10 Hz) oscillations (Chrobak and Buzsaki, 1998). We recorded membrane potential and membrane current responses to either 1 s trains of single stimuli at theta frequency (10 Hz) or brief trains of gamma frequency stimuli (either 40 Hz or 80 Hz, 50 ms duration) repeated at theta frequency for 1 s. Since responses showed short-term synaptic plasticity that stabilized within two or three theta cycles, we focus here only on responses during the final 500 ms of the stimulus train. In this time window responses to 10 Hz stimulation, and responses to brief gamma trains repeated at 10 Hz, had similar average amplitudes and were followed by a return to baseline (data not shown). By contrast, the membrane potential response within each gamma frequency stimulus train varied steeply as a function of neuronal location. In the most dorsal neurons, membrane potential responses to gamma frequency stimulus epochs showed little summation (Figure 3A), whereas summation of the gamma frequency responses became progressively larger for neurons at increasingly more ventral locations (Figure 3B). The dependence on dorsal-ventral location was steeper for inputs activated at 80 Hz (slope = 0.75 mm^{-1}, $R^2 = 0.58$, $p = 0.0016$) (Figure 3D) compared with inputs activated at 40 Hz (slope = 0.2 mm^{-1}, $R^2 = 0.37$, $p = 0.016$) (Figure 3C).

Since short-term synaptic plasticity could cause differences in summation of synaptic inputs, we also made voltage-clamp recordings to examine the corresponding synaptic current responses. In contrast to the steep dorsal-ventral gradient in summation of EPSPs, we found no dependence on location of summation of the corresponding EPSCs activated at either 40 Hz (slope = 0.009 mm^{-1}, $R^2 = -0.09$, $p = 0.92$) or 80 Hz (slope = 0.088 mm^{-1}, $R^2 = -0.02$, $p = 0.41$) (Figures 3C and 3D). As a further test we minimized variability in the EPSC amplitude by selecting only neurons for which the final EPSC during the gamma epoch was within 20% of the amplitude of the first EPSC (open circles in Figures 3C and 3D). In this case the steep gradient in EPSP summation was maintained for responses to 40 Hz (slope = 0.18 mm^{-1}, $R^2 = 0.70$, $p = 0.0032$) and 80 Hz (slope = 0.69 mm^{-1}, $R^2 = 0.62$, $p = 0.021$) stimulus epochs. Thus, these data indicate that stellate neurons at different dorsal-ventral locations show systematic differences in their responsiveness to gamma frequency inputs that are not explained by differences in synaptic transmission.

Together, these data indicate that the EPSP waveform, the time window for detection of coincident synaptic responses, and the integration of gamma frequency synaptic inputs depend on a neuron's location within the MEC. Importantly, the progressive slowing of temporal integration of synaptic inputs along the dorsal-ventral axis of the MEC maps onto the increasing spacing of grid fields found during recordings made in behaving animals from neurons in the same region (Brun et al., 2008; Hafting et al., 2005).

Intrinsic Membrane Properties of Stellate Cells Vary with Dorsal-Ventral Location

What are the cellular mechanisms responsible for the dorsal-ventral gradient in synaptic integration? Since differences in synaptic currents do not appear to account for the dorsal-ventral gradient in the EPSP waveform, we investigated nonsynaptic

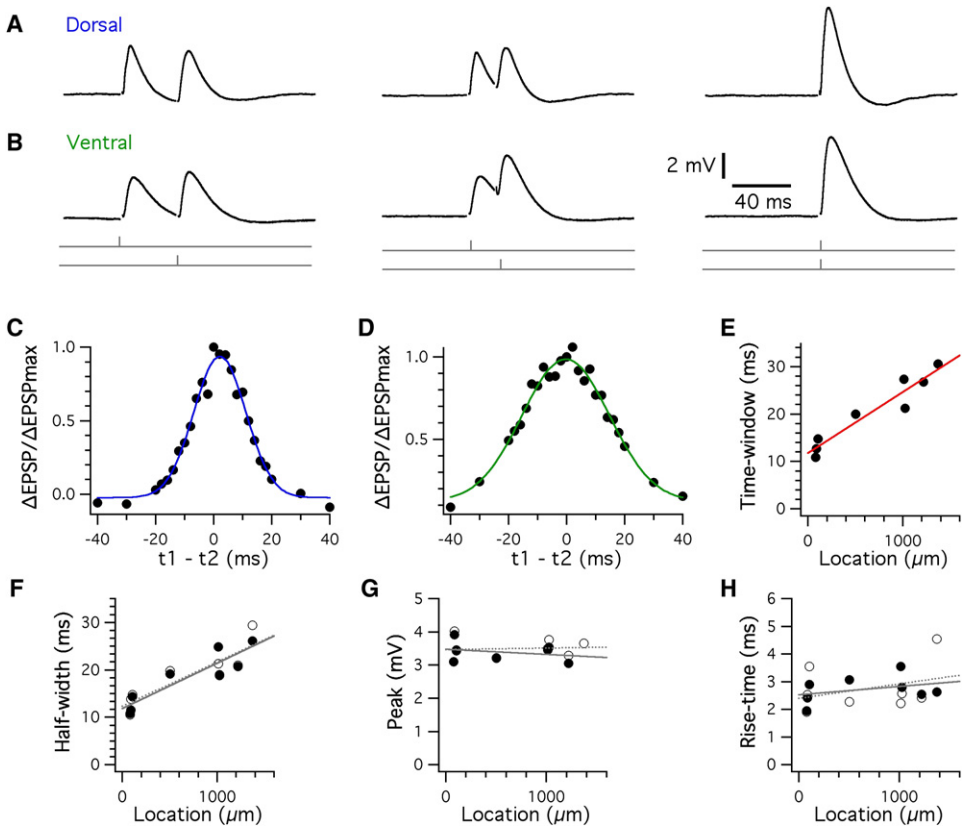

Figure 2. The Time Window for Integration of Synaptic Inputs Varies with Location

(A and B) Examples of experiments to evaluate the time window for integration of synaptic inputs evoked by stimulation of two independent pathways. EPSPs were evoked in each pathway with an interval of 40 ms (left column), 20 ms (middle column), and 0 ms (right column). The dorsal neuron has a location of 113 μm and the ventral neuron has a location of 1025 μm.

(C and D) Summation plotted as a function of the relative time between stimulation of the two pathways. The data points are fitted with a Gaussian function (line).

(E) The width of the Gaussian describing the time window for synaptic integration is plotted as a function of location along the dorsal-ventral axis of the MEC. The red line is a linear fit (R^2 = 0.9 and p = 0.0002).

(F–H) The half-width (dorsal pathway: R^2 = 0.74, p = 0.004; ventral pathway: R^2 = 0.80, p = 0.002) (F), mean amplitude (dorsal pathway: R^2 = −0.16, p = 0.85; ventral pathway: R^2 = −0.11, p = 0.6) (G), and 20%–80% rise time (dorsal pathway: R^2 = −0.04, p = 0.43; ventral pathway: R^2 = −0.03, p = 0.4) (H) of evoked EPSPs are plotted as a function of location along the dorsal-ventral axis of the MEC. There is no significant difference between the amplitude, rise time, or half-width of EPSPs evoked with stimulating electrodes placed in layer I dorsal (open circles) or ventral (closed circles) to the recorded neuron (p > 0.4).

integrative properties of stellate neurons. To do this independently of synaptic activation, we evaluated membrane potential responses to current steps applied to stellate neurons from different locations along the dorsal-ventral axis of the MEC.

To produce a given displacement of the membrane potential from rest required introduction of larger currents into neurons located at the dorsal end of the MEC (Figure 4A) than those in neurons from more ventral locations (Figure 4B). Estimates obtained from these experiments of membrane input resistance (slope = 18.3 MΩ mm^{-1}, R^2 = 0.62, p << 1e−6) and membrane time constant (slope = 5.5 ms mm^{-1}, R^2 = 0.48, p << 1e−6) increased steeply from the dorsal to the most ventral locations within the MEC (Figures 4C and 4D). By contrast, the resting membrane potential was independent of dorsal-ventral location (R^2 = −0.009, p = 0.59) (Figure 4E). Stellate neurons at all locations along the dorsal-ventral axis of the MEC demonstrated characteristic membrane potential "sag" and "rebound" responses (Figures 4A and 4B), which are mediated by activation and deactivation of HCN channels (Dickson et al., 2000; Nolan et al., 2007). While the relative amplitude of the membrane potential sag decreased with distance from the dorsal pole, this gradient was shallower than those for input resistance and time constant (R^2 = 0.18, p = 2.8e−5) (Figure 4F). This striking anatomical organization of the integrative properties of stellate cells extended to measures of suprathreshold excitability. Thus, consistent with these cells' lower input resistance, the minimum amplitude of positive current steps required to evoke action potentials was much larger for neurons from dorsal locations as compared to that for ventral locations (R^2 = 0.78, p = 3.8e−6) (Figures 4G and 4H). Importantly, while the current threshold for spiking decreased approximately 4-fold along the dorsal-ventral axis of the MEC (Figure 4I), the waveform of the action potential and the voltage threshold for action potential initiation did not depend on location (p > 0.25) (Figures 4J–4L), indicating that the gradient

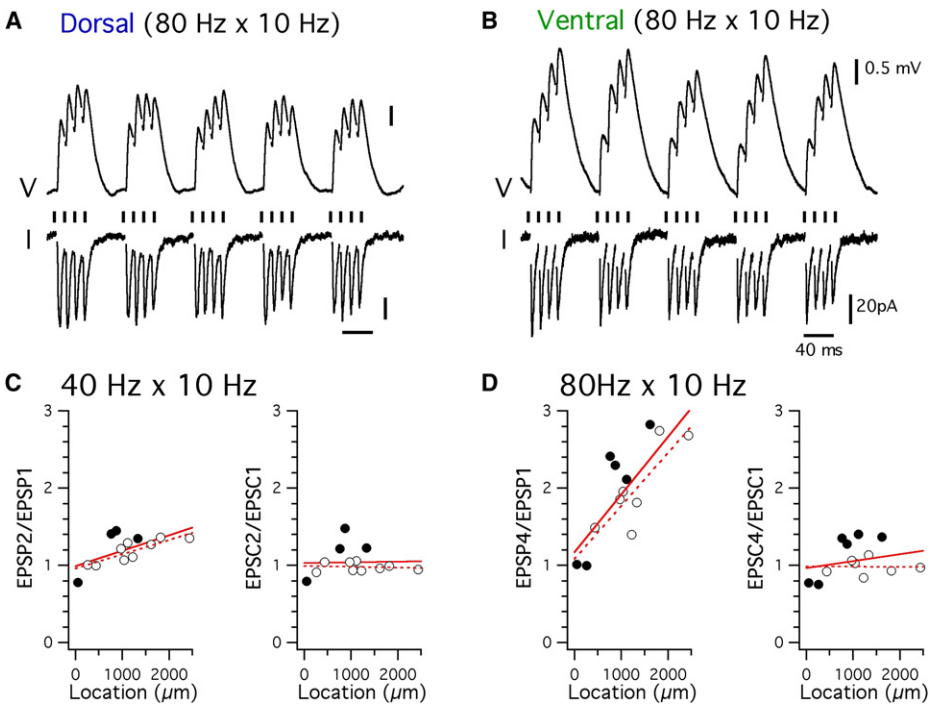

Figure 3. Summation of Gamma Frequency EPSP Trains Varies as a Function of Dorsal-Ventral Location

(A and B) Examples of synaptic potential (top) and synaptic current (bottom) responses of dorsal (A) and ventral (B) stellate neurons to epochs of 80 Hz gamma frequency stimulation nested within theta frequency trains. Vertical bars indicate times of synaptic stimulation. Traces are normalized to the peak of the first synaptic response. The dorsal neuron is 440 μm and the ventral neuron 1819 μm from the dorsal border of the MEC.

(C and D) EPSP (left) and EPSC (right) summation is plotted as a function of dorsal-ventral location for responses to 40 Hz (C) or 80 Hz (D) gamma stimulation. Summation is measured as the peak membrane potential or current displacement from rest during the second (C) or fourth (D) EPSP or EPSC in each gamma epoch divided by the peak of the first EPSP or EPSC. Open circles indicate the subset of experiments for which the fourth EPSC peak was within 20% of the amplitude of the first EPSC peak, solid lines indicate fits to the complete data set, and dashed lines indicate fits to the subset of experiments with minimal variation between consecutive EPSCs.

in current threshold is not secondary to changes in the spike generation mechanism, but rather reflects differential integration of the injected current.

Since background synaptic activity can modify the resting integrative properties of some neurons, we carried out similar experiments in the presence of blockers of ionotropic glutamate and GABA receptors (Figures 4M–4O). Again, we found that input resistance (R^2 = 0.62, p << 1e−6) (Figure 4M), membrane time constant (R^2 = 0.39, p << 1e−6) (Figure 4N), and current threshold for action potential generation (R^2 = 0.42, p << 1e−6) (Figure 4O) vary steeply as a function of location, whereas the resting potential and spike properties were independent of location (data not shown), indicating that the gradients in membrane properties are not a result of differences in background synaptic activation. Consistent with this conclusion, the gradients in input resistance (R^2 = 0.49, p = 0.048, n = 7) and current threshold (R^2 = 0.67, p = 0.03, n = 6) were maintained when synaptic transmission was abolished using a modified ACSF containing reduced Ca^{2+} and elevated Mg^{2+} (data not shown).

To assess whether these integrative properties of stellate neurons vary continuously with location, as has been found for the dorsal-ventral organization of grid cell spacing (Brun et al., 2008), or if instead they reflect a modular organization, we reevaluated our largest data set, which is from recordings made in the presence of blockers of ionotropic glutamate and GABA receptors (Figures 4M–4O). Grouping the data in 500 μm length bins indicates a progressive change in the membrane properties of stellate neurons from bin to bin, which is consistent with a linear gradient (Figures 4M–4O). Nevertheless, this analysis does not rule out step-like changes or modular organization at finer spatial scales than the bin width of 500 μm.

Variation in Stellate Neuron Morphology with Dorsal-Ventral Location

Differences between neurons in their intrinsic integrative properties could arise either through differences in the density or properties of ion channels in their membranes, or through differences in their morphology. To distinguish between these possibilities, we first reconstructed the morphology of the neurons that we recorded from. The morphology of stellate neurons along the full extent of the dorsal-ventral axis was similar to previous descriptions from other species (Figures 5A–5C) (Buckmaster et al., 2004; Klink and Alonso, 1997). Primary dendrites extended in all directions from the cell body, while axons projected directly through the deep layers of the MEC toward the hippocampus. In many cases, axons had collaterals that branched extensively

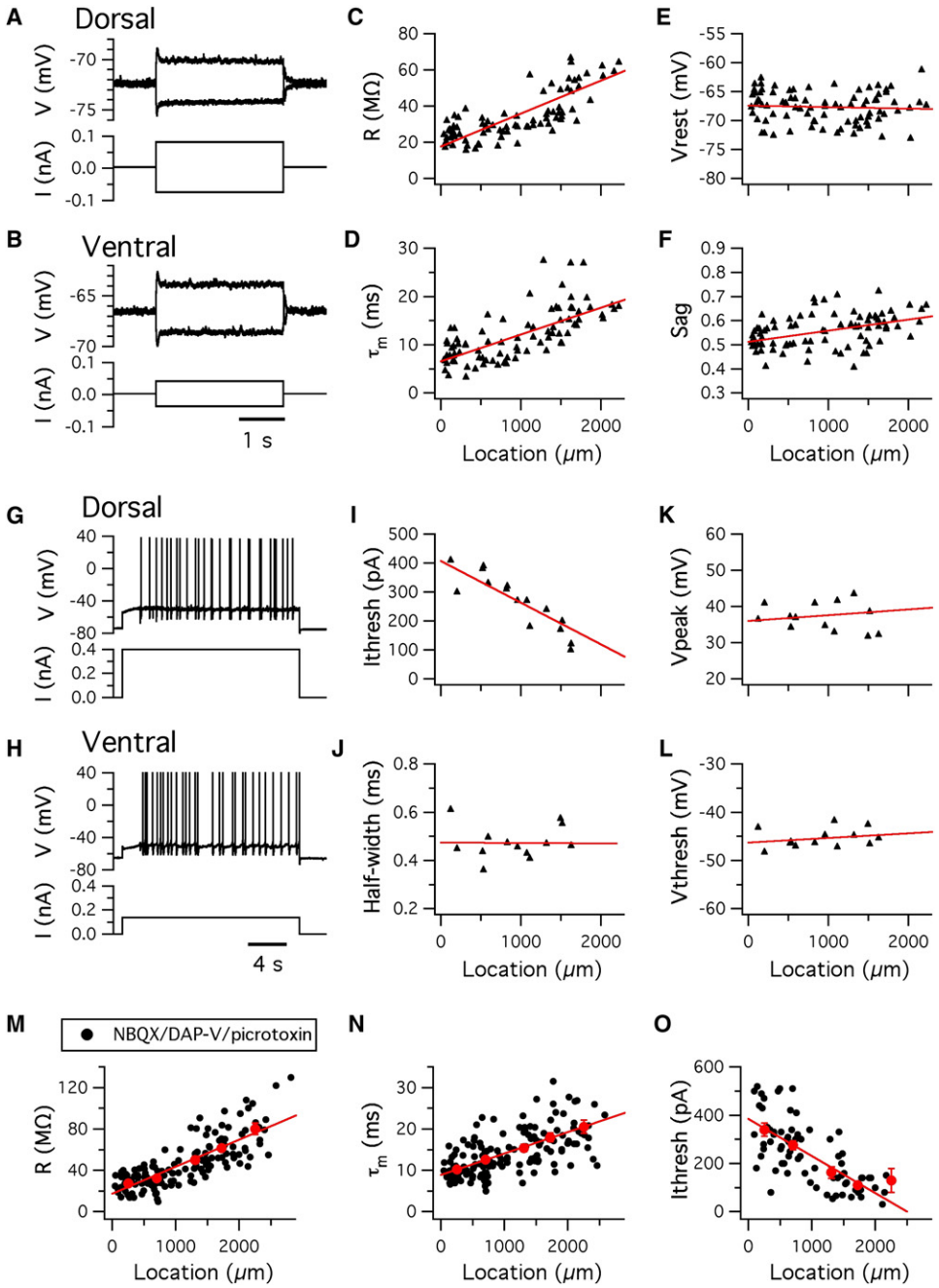

Figure 4. The Resting and Excitable Properties of Stellate Cells Vary along the Dorsal-Ventral Axis of the MEC

(A and B) Examples of membrane potential responses (upper traces) to current steps (lower traces) recorded from stellate cells located in the dorsal (A) (location 127 μm) and ventral (B) (location 1586 μm) entorhinal cortex.

(C–F) Input resistance (C), membrane time constant (D), resting membrane potential (E), and membrane potential sag (F), plotted as a function of cell body location along the dorsal-ventral axis of the entorhinal cortex. In all panels, red lines indicate linear fits to the data.

(G and H) Examples of threshold responses to positive current steps recorded from stellate cells located in dorsal (G) (location 324 μm) and ventral (H) (location 1629 μm) parts of the MEC.

(I–L) Current threshold (I), action potential half-width (J), peak action potential depolarization (K), and voltage threshold (L), plotted as a function of cell body location along the dorsal-ventral axis of the MEC.

(M–O) Input resistance (M), membrane time constant (N), and current threshold (O) are plotted as a function of location for individual stellate cells (black circles) recorded in the presence of NBQX (5 μM), D-APV (50 μM), and picrotoxin (50 μM). Also plotted are mean values for data binned at 500 μm intervals (red circles). Error bars = SEM.

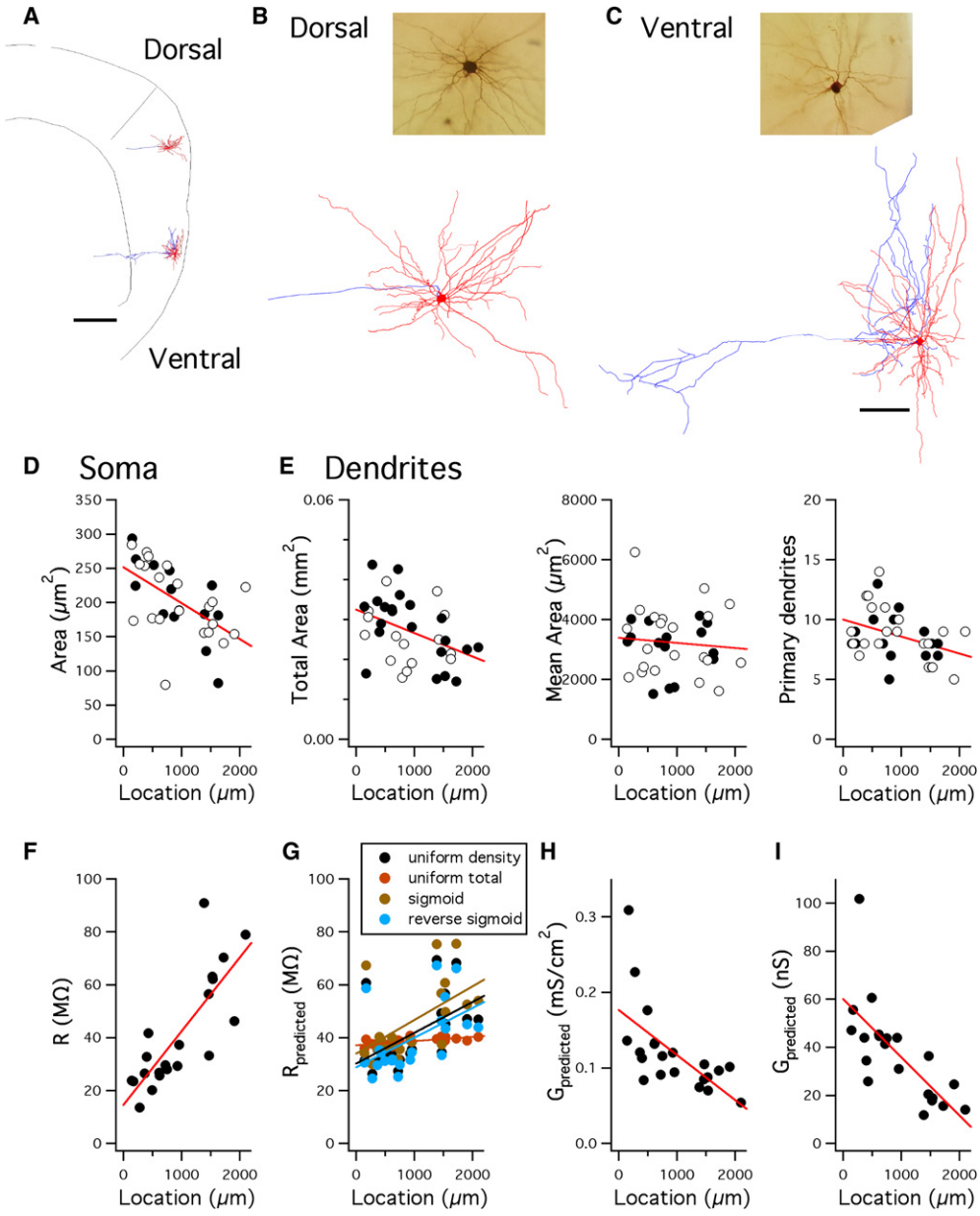

Figure 5. Organization of Stellate Cell Morphology along the Dorsal-Ventral Axis of the MEC Does Not Fully Account for the Dorsal-Ventral Organization of Integrative Properties

(A) Parasagittal outline of the caudal brain illustrating the location of example stellate cells from the dorsal and ventral poles of the MEC. (B and C) Neurolucida reconstructions and photomicrographs (inset) of the dorsally (B) and ventrally (C) located stellate cells from (A). Scale bars are 500 μm (A) and 100 μm (B and C). (D) The cross-sectional soma area of reconstructed stellate cells plotted as a function of the location of their soma along the dorsal-ventral axis of the entorhinal cortex. (E) The total dendritic surface area (left), average dendritic surface area (middle), and number of primary dendrites (right) for the reconstructed stellate cells plotted as a function of soma location. In (D) and (E), open circles are cells recorded in blockers of fast synaptic transmission and further analyzed in (F)–(I) (n = 21), while closed circles are neurons recorded in the absence of blockers (n = 15). Lines indicate linear fits of the data. (F) Membrane input resistance plotted as a function of location for the subset of neurons in (D) and (E) from which recordings were made in the presence of antagonists for ionotropic glutamate and GABA receptors. The fit indicates a gradient of 27.9 MΩ mm^{-1} (R^2 = 0.62, p = 1.5e−5). (G) Input resistance plotted as a function of location for model neurons generated from the reconstructed cells in (F), with each cell containing an identical uniform leak conductance density of 0.1 mS/cm^2 (slope = 11.6 MΩ mm^{-1}, R^2 = 0.26, p = 0.01), an identical uniform total leak conductance of 25 nS (slope = 1.6 MΩ mm^{-1}, R^2 = 0.47, p = 3.9e−4), a leak conductance with a sigmoid distribution (slope = 12.8 MΩ mm^{-1}, R^2 = 0.27, p = 0.009), or a leak conductance with a reverse sigmoid distribution (slope = 11.1 MΩ mm^{-1}, R^2 = 0.24, p = 0.013). (H and I) Predicted leak conductance density (H) and total leak conductance (I) plotted as a function of location when the uniform leak conductance of each model neuron is adjusted to reproduce the experimentally measured input resistance. A linear fit of the leak conductance has a slope of −6.0 mS cm^{-2} mm^{-1} (R^2 = 0.37, p = 0.02), while a linear fit of the total conductance has a slope of −24.1 nS mm^{-1} (R^2 = 0.49, p = 2.6e−4).

within layer II and layer V/VI, suggesting anatomical substrates for recurrent network activity within layer II (Kumar et al., 2007) and a direct influence of stellate cells on layer V/VI neurons. Quantification of morphological properties that might impact the measured electrophysiological properties of stellate neurons indicates that the total dendritic surface area (R^2 = 0.15, p = 0.011) as well as the cell body cross-sectional area (R^2 = 0.42, p = 1.5e−4) and the cell body perimeter (R^2 = 0.34, p = 8.1e−4) decrease with distance from the dorsal pole of the MEC (Figures 5D and S2). The reduction of total dendritic surface area at progressively more ventral locations is not due to differences in the surface area of individual dendritic trees (R^2 = −0.02, p = 0.59), but instead reflects a decrease in the number of primary dendrites (R^2 = 0.12, p = 0.021), which was accompanied by a reduction in the total number of dendritic branch points (R^2 = 0.2, p = 0.0036) (Figures 5E and S2). We did not find any significant effect of dorsal-ventral location on the axonal length (R^2 = 0.024, p = 0.19) or number of axonal branch points (R^2 = −0.0046, p = 0.36) (Figure S2).

While these data suggest that the morphology of stellate neurons varies with dorsal-ventral location in the MEC, it is unclear if these differences can account for differences between the integrative properties of stellate neurons at different locations. In particular, the dendrites of a stellate neuron might be expected to dominate its integrative properties because of their large surface area (Figure S3). Yet, the relative change in input resistance with location along the dorsal-ventral axis of the MEC (Figures 4C and 4M) is much steeper than the corresponding change in total dendritic surface area or number of primary dendrites (Figure 5E). Therefore, to clarify the possible influence of morphology, we generated multicompartment computational models from reconstructions of neurons that were recorded from in the presence of blockers of ionotropic glutamate and GABA receptors. Just as for the larger population of neurons (Figure 4), this subset of 21 neurons also demonstrated a steep gradient in their resting input resistance (slope = 27.9 MΩ mm^{-1}, R^2 = 0.62, p = 1.5e−5) (Figure 5F).

If changes in neuronal morphology alone are sufficient to explain differences in integrative properties with dorsal-ventral location, then introduction of the same membrane conductance into all of the reconstructed neurons should reproduce the experimentally observed gradient in input resistance. Since the subcellular distribution of membrane ion channels in MEC stellate cells is not known, we evaluated the models using several different rules for distribution of the membrane conductance across the cell body and dendrites (see Experimental Procedures). As the goal was to estimate the consequences of a change in the membrane conductance, rather than study the voltage dependence of subthreshold responses, we did not include detailed biophysical ion channel mechanisms in the models, but instead used a single passive membrane conductance. None of the simulations were able to reproduce the experimentally measured dorsal-ventral gradient in the input resistance of stellate neurons (Figure 5G). The closest match to the experimental data was obtained with a sigmoid distribution of the membrane conductance, which predicted a gradient in input resistance with slope of 12.8 MΩ mm^{-1} (R^2 = 0.27, p = 0.009), which is less than half the experimentally measured gradient for these neurons. A reverse sigmoid and uniform distribution of the membrane conductance predicted gradients similar to the sigmoid distribution of the membrane conductance, while the prediction furthest from the experimental data, obtained when the total leak conductance was held constant (slope = 1.6 MΩ mm^{-1}, R^2 = 0.47, p = 3.9e−4), was less than one-tenth of the experimentally measured gradient (Figure 5G). Thus, these simulations predict that differences in morphology of stellate neurons are unable to fully account for the dorsal-ventral gradient in the input resistance.

Since these simulations indicate that differences in morphology are unlikely to fully explain the organization of the integrative properties of stellate neurons, we carried out a further set of simulations to instead ask, what is the membrane conductance for each model neuron that results in its input resistance being equal to that measured experimentally? These simulations predict that the experimentally observed gradient in the input resistance of stellate neurons requires a progressive decrease in the density of the membrane conductance (Figure 5H) and in the total membrane conductance (Figure 5I) correspondent to neuronal location along the dorsal-ventral axis of the MEC. Similar predictions were obtained for each subcellular distribution of the membrane conductance (data not shown).

Differential Effects of Ion Channel Blockers on the Input Resistance Gradient

Does the gradient in resting membrane conductance predicted by our simulations exist, and if so, what are the ion channels responsible? Since we previously found that HCN channels, which mediate the hyperpolarization-activated current (I_h), strongly influence the resting conductance of stellate neurons (Nolan et al., 2007), we first examined whether block of HCN currents with ZD7288 (BoSmith et al., 1993) alters the gradient in input resistance. Perfusion of ZD7288, at a concentration that fully blocks I_h in stellate neurons (Nolan et al., 2007 and Figure 7), hyperpolarized their membrane potential and increased their input resistance. The input resistance gradient was maintained in the presence of ZD7288, indicating that HCN currents are not required to maintain the gradient in integrative properties of stellate neurons (Figure 6A). The relative change in input resistance caused by ZD7288 was consistent along the dorsal-ventral axis, becoming slightly smaller with increasing distance from the dorsal border of the MEC (p = 0.048). Based on the predictions of our model in Figures 5I and 5J, this suggests that HCN current density has a slightly steeper dependence on dorsal-ventral location than the total membrane conductance does, but that at least one other membrane conductance must contribute to the input resistance gradient.

Since the dorsal-ventral input resistance gradient remained after block of I_h, we were able to evaluate the location dependence of the membrane time constant without contamination by I_h. Thus, we estimated the membrane time constant using a fitting method that accounts for the relatively rapid spread of current from the soma into the dendrites (Rall, 1960). This analysis also demonstrated a dorsal-ventral gradient in the membrane time constant (p = 0.015) (Figure S4). As differences in the membrane capacitance are unable to explain a gradient in input resistance, this provides further support to the conclusion

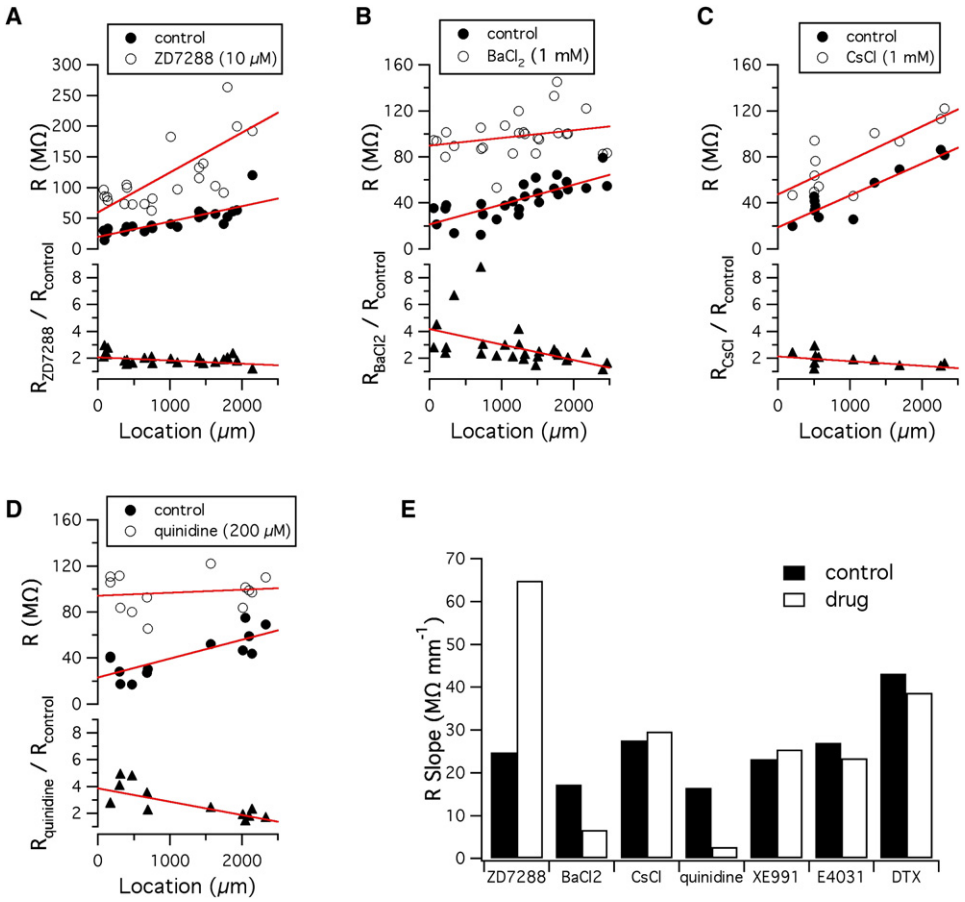

Figure 6. Differential Actions of HCN and K^+ Channel Blockers on the Dorsal-Ventral Input Resistance Gradient

(A–D) Input resistance (upper plots) and relative change in input resistance (lower plots) are plotted as a function of location for stellate neurons recorded in control conditions and in the presence of specified ion channel blockers. (A) Input resistance depends on location in control conditions (gradient = 24.8 MΩ μm^{-1}, R^2 = 0.62, p = 9.3e−6) and presence of 10 μM ZD7288 (gradient = 64.9 MΩ μm^{-1}, R^2 = 0.46, p = 0.0003), but the effect of ZD7288 on input resistance varies slightly as a function of location (slope = −0.2 μm^{-1}, R^2 = 0.14, p = 0.048). The change in membrane potential caused by ZD7288 was independent of neuronal location (p = 0.19) (not shown). (B) The dependence of input resistance on location for stellate cells recorded in control conditions is abolished in the presence of 1 mM $BaCl_2$ (control: R^2 = 0.58, gradient = 17.3 MΩ mm^{-1}, p = 4.2e−06; $BaCl_2$: R^2 = 0.02, gradient = 6.6 MΩ mm^{-1}, p = 0.21), which causes a greater increase in the input resistance of more dorsal (as compared with more ventral) neurons (slope = −1.1 μm^{-1}, R^2 = 0.21, p = 0.011). (C) One millimolar CsCl (control, R^2 = 0.82, p = 8.2e−05; CsCl, R^2 = 0.60, p = 0.003). (D) Two-hundred micromolar quinidine (control: R^2 = 0.58, p = 0.001; quinidine: R^2 = −0.07, p = 0.62). There was a significant relative change in input resistance as a function of location for quinidine (p = 0.003), but not for CsCl (p = 0.1). Input resistance in the presence of ion channel blockers was calculated after adjusting the membrane potential to the control resting value by injection of constant current.

(E) The slope of the linear fit of the relationship between input resistance and location in control conditions and in the test drug, for each group of experiments to evaluate the actions of ion channel blockers.

that the membrane conductance of stellate neurons varies according to their dorsal-ventral location.

The hyperpolarized membrane potential after block of I_h suggests that K^+ channels may contribute to the remaining membrane conductance. We therefore examined the consequences of blocking K^+ channels. The gradient in input resistance was abolished in the presence of 1 mM Ba^{2+}, which is effective at blocking inwardly rectifying (KCNJ) and two-pore-domain (KCNK) K^+ channels, as well as a number of voltage-gated K^+ channels (Figure 6B) (Coetzee et al., 1999; Goldstein et al., 2005; Kubo et al., 2005). The relative change in input resistance caused by Ba^{2+} decreased as a function of a neuron's location along the dorsal to ventral axis (p = 0.01) (Figure 6B). This is inconsistent with the input resistance gradient being due solely to a difference in neuronal morphology, but rather supports the idea that there is a dorsal-ventral organization of membrane ion channels that can be manipulated pharmacologically.

To identify likely candidate K^+ channels that are open at rest, we used the Allen Brain Atlas (Lein et al., 2007) to evaluate mRNA expression within the superficial layers of the MEC. Subunits of the M current (KCNQ), ERG (KCNH), Kv1 (KCNA), KCNJ, and two-pore-domain ion channels all appear to be expressed in layer II of the MEC (Table S1 available online). However, the resting input resistance was relatively unaffected and the dorsal-ventral gradient was maintained after blocking the former channels with XE991, E4031, or α-DTX, respectively, although

α-DTX causes a small reduction in input resistance that appeared to depend on location (Figures 6E and S5). Similarly, the input resistance gradient was maintained in 1 mM Cs^+ (Figure 6C), which blocks KCNJ K^+ channels, but not two-pore-domain ion channels (Coetzee et al., 1999; Goldstein et al., 2005; Kubo et al., 2005). By contrast, the gradient was abolished by 200 μM quinidine, which blocks a number of ion channel types including two-pore-domain ion channels, but not KCNJ K^+ channels (Coetzee et al., 1999; Goldstein et al., 2005; Kubo et al., 2005) (Figure 6D). Thus, these pharmacological data indicate that ion channels that are sensitive to XE991, E4031, α-DTX, or Cs^+ are not required for the dorsal-ventral gradient in input resistance, but rather point toward roles for ion channel subtypes that are sensitive to quinidine and Ba^{2+} (Figure 6E).

Dorsal-Ventral Gradients in a Leak K^+ Current and a Hyperpolarization-Activated Current

We conducted voltage-clamp recordings to explore the biophysical properties of I_h and the Ba^{2+}- and quinidine-sensitive membrane conductance. The recording conditions were modified to facilitate isolation of the targeted membrane conductance by blocking ion channels that might otherwise mediate potentially confounding secondary actions (see Experimental Procedures); for example, depolarization induced by Ba^{2+} might otherwise alter activation of voltage-gated ion channels in poorly clamped distal dendrites or cause release of neurotransmitter from presynaptic neurons.

Hyperpolarizing voltage steps evoked slowly activating inward currents that were blocked by ZD7288 and had properties similar to previous descriptions of I_h recorded from stellate neurons (Figures 7A, 7B, and S6) (Dickson et al., 2000; Nolan et al., 2007). The amplitude of I_h, quantified either from the ZD7288-sensitive current (Figure 7A) or from tail currents following hyperpolarizing voltage steps (Figure S6), decreased with increasing distance from the dorsal border of the MEC ($p = 0.0049$ and $p = 0.0044$, respectively). Estimates of the voltage dependence and time course of I_h did not vary with location (Figure S6). Importantly, the relative change in the amplitude of I_h was much steeper than expected for a conductance with identical density in all stellate neurons, but was comparable to the expected gradient for a conductance that contributes to the dorsal-ventral organization of input resistance (cf. Figure S7).

At a holding potential of −70 mV, both Ba^{2+} and quinidine blocked an outward current (Figures 7C and S8). The amplitude of the Ba^{2+}-sensitive ($p = 0.023$) and quinidine-sensitive ($p = 0.0004$) outward current varied systematically with location along the dorsal-ventral axis (Figures 7D and S8). Large-amplitude currents were present in dorsal neurons, whereas the current was almost completely absent from the most ventrally located neurons. A similar gradient was found when currents were measured from responses to slow ramp-like changes in membrane potential or from responses to voltage steps (Figure S8). The responses to voltage steps did not suggest time-dependent gating of the current (Figure S8). While the currents sensitive to quinidine and Ba^{2+} demonstrate shallow voltage dependence, the current remaining in the presence of either blocker was voltage independent, indicating that activation of voltage-gated ion channels was blocked by the modified ACSF used for these experiments.

The currents blocked by quinidine and Ba^{2+} had reversal potentials of −94.2 ± 2.0 mV (n = 14) and −95.5 ± 2.6 mV (n = 17), respectively, which is close to the estimated reversal potential for K^+ of around −105 mV. Consistent with a role for K^+ channels, the reversal potential of the quinidine-sensitive current was modified by altering the extracellular K^+ concentration. Thus, in ACSF in which the calculated K^+ reversal is approximately −70 mV, the quinidine-sensitive current had an estimated reversal potential of −72.9 ± 0.87 mV (n = 5, data not shown). The reversal potential did not vary as a function of location (quinidine, $p = 0.12$; $BaCl_2$, $p = 0.73$). Just as for the gradient in I_h, the relative dorsal-ventral change in the amplitude of the quinidine- and Ba^{2+}-sensitive currents was too steep to be accounted for by differences between the morphologies of stellate neurons (cf. Figure S7). Together, these data provide evidence for dorsal-ventral gradients in both a leak K^+ conductance and an HCN conductance expressed by stellate cells within the MEC.

Topographical Organization of Ion Channel Properties Accounts for the Dorsal-Ventral Gradient in Synaptic Integration

Does dorsal-ventral organization of the membrane conductance in stellate neurons explain the differences in synaptic integration along the dorsal-ventral axis of the MEC? If this is the case, then the dorsal-ventral organization of the membrane conductance predicted by our earlier simulations of reconstructed neurons should also account for the waveform of synaptic responses. Consistent with this prediction, simulations with the reconstructed stellate neurons demonstrate that when the membrane conductance is adjusted to account for the dorsal-ventral gradient in input resistance as in Figures 5H and 5I, then the rise time ($R^2 = 0.38$, $p = 0.0017$) and half-width ($R^2 = 0.49$, $p = 0.00024$) of EPSPs generated by the model follow an increase with distance from the dorsal border of the MEC (Figures 8A and 8B). Replacing the passive membrane conductance with the same total membrane conductance density composed of a combination of I_h, a leak K^+, and a leak Na^+ conductance (see Experimental Procedures) also reproduced the dorsal-ventral gradient in the EPSP waveform (Figures 8A and 8B). The organization of the EPSP waveform predicted by these simulations is remarkably similar to that seen in the experimental data (Figure 1). By contrast, when the model neurons at all locations have the same membrane conductance, then the rise times ($R^2 = -0.044$, $p = 0.7$) and half-widths ($R^2 = 0.02$, $p = 0.24$) of the simulated EPSPs are completely independent of the neuron's dorsal-ventral location (Figure 8C). Importantly, as these simulations are constrained by reconstructions of neuronal morphology and experimental measurements of input resistance, but not by recordings of synaptic responses, they demonstrate that the dorsal-ventral organization of the membrane conductance suggested by our analysis of the responses of stellate neurons to injected current is able to account for the dorsal-ventral organization of the integration of synaptic inputs by stellate neurons.

Finally, we asked if blocking I_h or the leak K^+ current modifies synaptic potentials. Consistent with our measurements of input resistance and membrane time constant after block of I_h, blocking I_h by intracellular dialysis of ZD7288 increased the duration of EPSPs, but the dorsal-ventral gradient in their half-width remained (Figure S9). We were unable to directly study the effects of Ba^{2+}

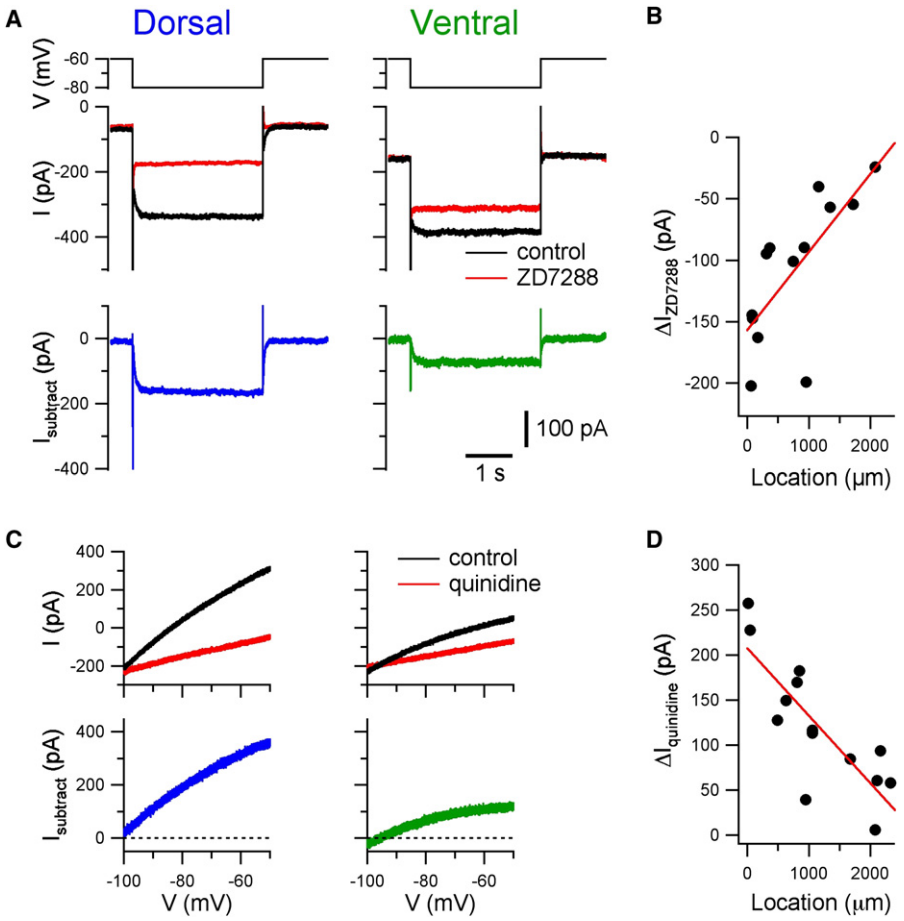

Figure 7. A ZD7288-Sensitive Conductance and a Quinidine-Sensitive Leak K^+ Conductance Follow a Dorsal-Ventral Gradient

(A) Examples of current response (middle traces) to voltage steps (upper traces) in control conditions and in the presence of ZD7288. Subtraction of the traces in ZD7288 from the control traces reveals the ZD7288-sensitive current (lower traces). The dorsal neuron is 63 μm and the ventral neuron 1347 μm from the dorsal border of the MEC.

(B) The amplitude of ZD7288-sensitive currents plotted as a function of location (slope = −63.7 pA μm^{-1}, R^2 = 0.48, p = 0.0049).

(C) Membrane current plotted as a function of membrane potential (upper plots) for stellate cells from the dorsal (left column) (location 17 μm) and ventral (right column) (location 2166 μm) MEC before and during perfusion of quinidine. The lower plots show quinidine-sensitive currents calculated by subtraction of the quinidine from the control traces. Currents are responses to 20 mV s^{-1} ramp changes in membrane potential.

(D) Amplitude of the quinidine-sensitive current at a membrane potential of −70 mV plotted as a function of location (gradient = −74.9 pA μm^{-1}, R^2 = 0.64, p = 0.0004).

or quinidine on evoked EPSPs, as bath application of quinidine impaired synaptic transmission and Ba^{2+} increased spontaneous synaptic transmission, while intracellular perfusion of either blocker had no effect on the resting membrane conductance. However, consistent with a role for a quinidine-sensitive current, the dependence on neuronal location of pseudo-EPSPs evoked by somatic injection of EPSC waveforms was abolished by quinidine (Figure S10F). Evaluation of the time window for integration of pairs of these injected EPSCs reveals a dependence on dorsal-ventral location that is also abolished by quinidine (Figures S10A–S10E).

DISCUSSION

We show that integration of synaptic inputs by stellate neurons varies with location along the dorsal-ventral extent of layer II of the MEC. This cellular variation corresponds closely to the dorsal-ventral organization of the spacing of grid fields recorded from MEC neurons in behaving animals. While we find evidence for dorsal-ventral organization of the morphology of stellate neurons, the gradient in synaptic integration appears to be accounted for by a corresponding organization of their membrane conductance. Our evidence suggests contributions of both leak K^+ channels and HCN channels.

Coordinated Control of Synaptic Integration within a Single Class of Cortical Neuron

With increasing distance from the dorsal boundary of the MEC, the spacing of grid-like firing fields of neurons in layer II increases (Brun et al., 2008; Fyhn et al., 2008; Hafting et al., 2005). We find a corresponding increase in the duration of EPSPs, a broadening

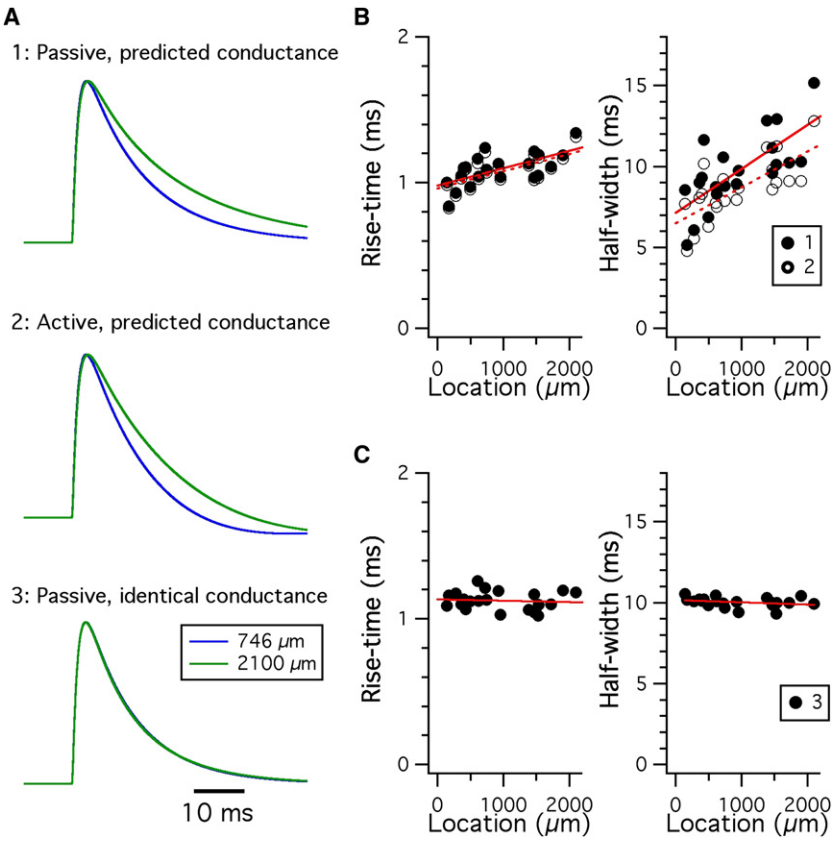

Figure 8. A Gradient in the Resting Membrane Conductance Accounts for the Dorsal-Ventral Organization of EPSP Waveforms

(A) Examples of average normalized EPSP waveforms from simulations of reconstructed dorsal and ventral neurons containing: 1: A passive membrane conductance with density predicted from the experimentally measured input resistance as in Figures 5H and 5I; 2: A separate leak and I_h conductance with total density as in (A1); 3: A passive membrane conductance with identical density in both neurons as in Figure 5G.

(B and C) The rise time (left) and half-width (right) of simulated somatic EPSPs are plotted as a function of dorsal-ventral location for reconstructed model neurons that contain a membrane conductance set as in (A1) ([B], closed circles) (rise time: slope = 0.119 ms mm^{-1}, R^2 = 0.38, p = 0.0017; half-width: slope = 2.7 ms mm^{-1}, R^2 = 0.49, p = 0.00024), as in (A2) ([B], open circles) (rise time: slope = 0.118 ms mm^{-1}, R^2 = 0.40, p = 0.0012; half-width: slope = 2.2 ms mm^{-1}, R^2 = 0.50, p = 0.00023) or as in (A3) (C) (rise time: slope = −9.3 μs mm^{-1}, R^2 = −0.04, p = 0.69; half-width: slope = −0.1 ms mm^{-1}, R^2 = 0.022, p = 0.24). The dependence on location of rise time and half-width differed significantly between the two passive conditions (ANOVA for rise time: condition, p = 0.0015; location, p = 0.00017; interaction, p = 0.0029; ANOVA for half-width: condition, p = 8.6e−5; location, p = 2.5 e−7; interaction, p = 4.0e−5).

of the time window for integration of independent synaptic inputs, and an increase in summation of gamma frequency synaptic trains recorded from stellate neurons in layer II of the MEC. These differences are not explained by alterations in synaptic transmission, synaptic location, or postsynaptic activation of neurotransmitter receptors (Figures 1 and 3), but are accounted for by differences in postsynaptic membrane properties of stellate neurons (Figures 4–8). These results support the idea that within a well-defined class of neuron, the rules that govern integration of synaptic inputs map onto the information encoded during behavior. However, it remains to be determined whether this putative principle could extend to other classes of neuron found in cognitive circuits.

Superimposed on the distinct dendritic morphology and the distinguishing electrophysiological signatures of stellate neurons, we find evidence for systematic differences in morphology and in membrane ion channels that are open at rest. Several lines of evidence indicate that differences in membrane ion channels are primarily responsible for the topographical organization of synaptic integration: (1) the input resistance, membrane time constant, and the amplitude of the threshold current required to evoke action potentials all vary according to a neuron's dorsal-ventral location. (2) Simulations with reconstructed neurons indicate that while differences in morphology could contribute to gradients in input resistance, they are unable to account for the dorsal-ventral organization of synaptic potential waveforms. Rather, these simulations predict a gradient in membrane conductance, which is able to explain the dorsal-ventral organization of the EPSP waveform. (3) Pharmacological manipulations can modify gradients in the membrane properties of stellate neurons and the time window for synaptic integration. (4) Voltage-clamp experiments reveal membrane conductance gradients predicted by our simulations. Together these results support a model whereby differences in the membrane conductances of stellate neurons organize synaptic integration along the dorsal-ventral axis of the MEC.

We find evidence that both HCN channels and leak K^+ channels contribute to the dorsal-ventral organization of synaptic integration. The pharmacology of the leak K^+ current is consistent with members of the KCNK family of two-pore-domain ion channels (Goldstein et al., 2001), and mRNA for five members of the KCNK family is expressed in the superficial MEC (Table S1). However, pharmacological tools do not allow clear discrimination of KCNK channels, and other K^+ channels could instead mediate this leak conductance (Goldstein et al., 2001). The mechanisms that mediate the organization of membrane conductance are also unclear, and our data are consistent with changes in the total number of ion channels or changes in channel open probability. Moreover, many other aspects of synaptic integration by stellate neurons remain to be investigated and our experiments do not rule out tuning of other properties to the spatial organization of grid fields; for example, dendritic nonlinearities that are inaccessible to measurement with somatic recordings.

Our observations of a dorsal-ventral gradient in the amplitude, but not the kinetics or voltage-dependence of I_h, as well as a gradient in input resistance, contrast with a recent study of stellate neurons from young rats, which reports a gradient in the fast time constant of I_h in the absence of corresponding gradients in input resistance or in the amplitude of I_h (Giocomo and Hasselmo, 2008). The differences may be explained by use here of older animals (age 29–66 days in the present study versus 17–23 days for Giocomo and Hasselmo), by differences in experimental procedures, differences in sex of the experimental animals (exclusively male in our study versus either sex in the previous study), or by use of different rodent species (mouse versus rat), although grid fields have a similar dorsal-ventral organization in both species (Hafting et al., 2005; Fyhn et al., 2008). In the study using young rats, some of the examples that suggest rapid activation of I_h with fast time constants of around 10 ms also suggest a slow outward current following maximal activation of the isolated I_h (Giocomo and Hasselmo, 2008). These properties are hard to reconcile with the known characteristics of mammalian HCN channels (Robinson and Siegelbaum, 2003) or with our recordings of I_h from stellate neurons (Nolan et al., 2007).

Functional Implications for Computations Carried Out within the MEC

What are the functional advantages of tuning synaptic integration? Neurons may adjust their integrative properties to the temporal or spatial organization of their synaptic inputs in order to encode information as efficiently as possible (Stemmler and Koch, 1999). In early stages of sensory processing, such a mechanism may reduce redundancy in the neural code (Laughlin, 1981). Alternatively, neurons that receive similar synaptic inputs may adapt their integrative properties in order to perform different computations. For example, differences in the time window for synaptic integration could determine how inputs are integrated relative to external pacemakers, such as the theta or gamma rhythm (Buzsaki, 2002), or could control the storage of information through spike-timing-dependent synaptic plasticity (Dan and Poo, 2004).

The dorsal-ventral organization of synaptic integration that we describe is consistent with abstract single-cell (Burgess et al., 2007) and network models for generation of grid-like firing fields (Moser et al., 2008). In both cases our data suggest biophysical constraints on how these models might be implemented. Thus, whereas dorsal neurons may be tuned to respond to coincident input, neurons located at increasingly more ventral locations appear to have broad time windows for coincidence detection of different inputs and allow temporal summation when the same input is activated repeatedly at gamma frequencies. These differences could be important for representation of information by spike timing relative to the ongoing theta rhythm (Hafting et al., 2008) and for responding to patterns of gamma frequency synaptic activity thought to occur in layer II of the MEC in behaving animals (Chrobak and Buzsaki, 1998). Testing these predictions will require new data about the source, patterns, and timing of synaptic input received by stellate neurons during spatial exploration. Identification of the molecular mechanisms that organize synaptic integration might then form a basis for investigating the behavioral roles of cellular computations carried out within the MEC and for determining whether deficits to the organization of synaptic integration could provide novel explanations for nervous system disorders.

EXPERIMENTAL PROCEDURES

Electrophysiology

Procedures for preparation of parasagittal brain slices were modified from Nolan et al. (2007) and are described in detail in Figure S1. The standard ACSF had the following composition: 124 mM NaCl, 1.2 mM NaH_2PO_4, 2.5 mM KCl, 25 mM $NaHCO_3$, 20 mM glucose, 2 mM $CaCl_2$, and 1 mM $MgCl_2$. For recording, slices were transferred to a submerged chamber and stellate neurons were visually identified under infrared illumination with DIC optics. Whole-cell recordings were obtained at 35°C–37°C from the soma of stellate neurons in MEC layer II using 2–5 MΩ resistance electrodes filled with intracellular solution comprising 130 mM KMethylsulfate, 10 mM KCl, 10 mM HEPES, 2 mM $MgCl_2$, 0.1 mM EGTA, 4 mM Na_2ATP, 0.3 mM Na_2GTP, and 10 mM phosphocreatine. Identification of stellate cells is described in Nolan et al. (2007) and in Figure S1. The intracellular solution usually also included biocytin (1%). Series resistances were <15 MΩ for voltage-clamp experiments and <40 MΩ for current-clamp experiments. There was no significant difference between the series resistance of recordings at different locations along the dorsal-ventral axis of the MEC (R^2 = 0.0079, p = 0.91). Series resistance in voltage-clamp recordings was compensated by 70%–80%. For current-clamp recordings appropriate bridge and electrode capacitance compensations were applied. Membrane current and voltage were filtered at 1–2 KHz and 4–20 KHz and sampled at 5–10 KHz and 10–50 KHz for voltage- and current-clamp experiments, respectively. An experimentally measured liquid junction potential of +8.1 mV (bath potential relative to the patch-pipette) for the standard ACSF was not corrected for.

Spontaneous EPSPs, recorded in the presence of D-APV to block NMDA receptors and in picrotoxin to block $GABA_A$ receptors, were abolished by 5 μM NBQX, indicating that they were mediated by AMPA/kainate receptors. Spontaneous EPSPs were detected using the template-matching algorithm built into Axograph X (http://axographx.com/) with parameters of noise standard deviation = 4, amplitude >0.5 mV, and rise time <3 ms. Evaluation of traces recorded in the presence of NBQX indicated a rate of detection fewer than five false positives during a 120 s recording.

Evoked EPSPs were recorded in the presence of 50 μM D-APV, 50 μM picrotoxin, and 1 μM CGP55845 to block $GABA_B$ receptors. While we focus on non-NMDA glutamatergic EPSPs, we also found a dorsal-ventral gradient in EPSP half-width without NMDA receptor blockade (R^2 = 0.63, p = 0.0021). Stimulating electrodes were placed in layer I, which contains axons from neocortical inputs and neurons in deeper layers of the MEC (Burwell, 2000; Dolorfo and Amaral, 1998). The stimulus strength was adjusted to evoke responses with a peak of approximately 3–4 mV. Only clearly isolated monosynaptic inputs, with invariant latency and rise time and absence of longer-latency synaptic potentials during their decay phase, were used for analysis. For dual pathway experiments, one stimulating electrode was placed approximately 300 μm dorsal and the other 300 μm ventral to the recorded cell. Independence of the two inputs was determined by comparing responses to the second of a pair of pulses separated by 20 ms, with responses to single stimuli. Whereas paired stimuli from the same electrode show facilitation, when the two stimuli were from different electrodes the second response was indistinguishable from responses in the absence of the preceding stimulus, indicating that the two stimulating electrodes activate independent pathways. To investigate responses to patterned synaptic inputs, we used three different stimulus trains of 1 s duration: theta trains contained ten stimuli at a frequency of 10 Hz; 40 Hz × 10 Hz trains contained epochs of two stimuli at 40 Hz repeated at a frequency of 10 Hz; 80 Hz × 10 Hz trains contained epochs of four stimuli at 80 Hz repeated at a frequency of 10 Hz. Current- and voltage-clamp recordings of responses to each input pattern were interleaved, while the stability of the input resistance and EPSP waveform were monitored and data rejected if changes of greater than ±20% occurred.

Measurement of quinidine- and Ba^{2+}-sensitive currents were made with the following cocktail of ion channel blockers and receptor antagonists added to

the ACSF: 0.01 mM ZD7288, 0.001 mM TTX, 1 mM Zn^{2+}, 5 mM 4-AP, 1 mM Cs+, 0.005 mM NBQX, 0.05 mM D-APV, and 0.05 mM picrotoxin (pH adjusted to 7.3 with HCl). Measurement of I_h was carried out in ACSF of the following composition: 115 mM NaCl, 1.2 mM NaH_2PO_4, 5 mM KCl, 25 mM $NaHCO_3$, 20 mM glucose, 2 mM $CaCl_2$, 1 mM $MgCl_2$, 1 mM $BaCl_2$, 0.1 mM $CdCl_2$, 1 mM 4-AP, 5 mM TEA, 0.005 mM NBQX, 0.05 mM picrotoxin, and 0.0005 mM TTX. One ventral neuron was excluded from the analysis of the reversal potentials as the quinidine-sensitive currents were too small for accurate estimates to be made.

Drugs were made fresh daily from frozen stocks concentrated $\geq$1000-fold, with the exception of quinidine (100 mM) and 4-AP (500 mM). Experiments to examine the effects of pharmacological block of ion channels on the gradient in input resistance were performed with blockers of ionotropic glutamate and GABA receptors added to the ACSF. During perfusion of K^+ channel blockers, particular care was also taken to prevent action potential firing by injection of negative current to maintain a membrane potential of −70 mV. All chemicals were purchased from Sigma (St. Louis, MO) with the exception of NBQX, D-AP5, ZD7288, and TTX from Ascent Scientific (Weston-super-Mare, UK); Picrotoxin, XE-991, and CGP55845A from Tocris Cookson (Bristol, UK); and E4031 and α-dendrotoxin from Alomone labs (Jerusalem, Israel).

For all experiments neuron location is expressed as the distance of the cell body from the dorsal border of the MEC (Figure S1). We estimate the dorsal-ventral extent of the MEC to be approximately 2200–2500 μm depending on the exact medial-lateral position of the brain slice. Qualitatively similar results were obtained when neuron location was instead measured as the distance between the cell body and the border between the postrhinal cortex and adjacent sensory cortex (area 36), or as a fraction of the estimated total length of the MEC. The locations of consecutive recordings were varied in order to interleave dorsal and ventral neurons.

Data Analysis

Electrophysiological data were analyzed in IGOR pro (Wavemetrics) using Neuromatic (http://www.neuromatic.thinkrandom.com/) and custom-written routines, or using Axograph. Statistical analysis was carried out using IGOR pro, Excel (Microsoft), or R (www.R-project.org). Mean values are ± standard error of the mean (SEM). Statistical significance was tested with linear regression, Student's t test, Wilcox test, ANOVA, or a General Linear Test as appropriate. Adjusted R^2 values are stated for results of linear regression. Qualitatively similar results were obtained with tests of correlation using Spearman's rank and Kendall's tau methods. Input resistance was calculated from the steady-state voltage ($\leq$5 mV) response to injected current steps ($\leq$100 pA). The membrane time constant was estimated either from the time constant of a single exponential fit to the voltage-response, or using a method that accounts for the rapid axial flow of current into the dendrites (Rall, 1960) (see Figure S4). Current threshold is defined as the amount of current ±5 pA required to elicit an action potential during a 3 s current step unless otherwise stated. Voltage threshold is the voltage just prior to the upshoot of the action potential.

The median age of mice used in the study was 43 days (range 29–66 days). We did not find any change in measured parameters with age of the mice. For example, in the largest data set, which was obtained in the presence of blockers of synaptic transmission, input resistance was independent of age ($R^2 = -0.0052$, p = 0.64, n = 150).

Reconstruction of Recorded Neurons

After recording, slices were fixed in 4% paraformaldehyde for at least 24 hr. Slices were then washed in phosphate-buffered saline followed by a 0.3% H_2O_2, 10% methanol solution. Tissue was then incubated in avidin-biotin horseradish peroxidase complex (ABC, Vector Laboratories, Burlingame, CA) for 48 hr. The biocytin-filled neurons were visualized using a 3, 3′-diaminobenzidine (DAB) substrate kit and slices were then mounted using Vectamount (Vector Labs). Neurons were traced using NeuroLucida software (MicroBrightField, Williston, VT) and a 100× oil immersion objective. Quantification of neuronal morphology was carried out using Neuroexplorer (MicroBrightField).

Simulations

Simulations were performed using the NEURON simulation environment (Carnevale and Hines, 2006). Full details of procedures used for simulations accompany Figure S3. For passive models in Figure 5G, a membrane conductance with a reversal potential of −70 mV was applied to the soma and dendrites following several different subcellular distribution rules: (1) The same membrane conductance of 0.0001 S cm^{-2} distributed uniformly throughout the soma and dendrites of each model cell (uniform density); (2) a constant total membrane conductance of 25 nS per cell, regardless of the neuron's size (uniform total); (3) a sigmoid increase in conductance with distance from the cell body (sigmoid); (4) a sigmoid decrease in conductance with distance from the cell body (reverse sigmoid). For models in Figures 5H and 5I, the membrane conductance was adjusted to account for the experimentally determined input resistance. For versions of the models that contained I_h, the membrane conductance density at the resting membrane potential of −70 mV was identical to that of the corresponding passive models. These models contained a passive leak K^+ conductance, a passive leak Na^+ conductance, and a simplified two-state model of I_h that approximates currents measured with voltage-clamp experiments (Nolan et al., 2007). The densities of the three conductances at −70 mV were chosen to account for the resting membrane potential and the change in input resistance caused by block of I_h, but qualitatively similar results are produced with a range of parameters.

SUPPLEMENTAL DATA

The supplemental data for this article include 10 Supplemental Figures and 1 Supplemental Table and can be found at http://www.neuron.org/supplemental/S0896-6273(08)00944-6.

ACKNOWLEDGMENTS

We thank Mayank Dutia and Stephen Williams for comments on an earlier version of the manuscript, Gareth Leng for statistical advice, and Jessie vanBinsbergen and Michelle Lew for assistance with reconstructions. This work was supported by the Medical Research Council (M.F.N. and C.O'D.), a Marie Curie Excellence grant (M.F.N.), the network of European Neuroscience Institutes (ENI-NET), a Human Frontier Science Program long-term fellowship (P.D.D.), and the EPSRC (C.O'D.).

Accepted: October 23, 2008
Published: December 10, 2008

REFERENCES

Alonso, A., and Klink, R. (1993). Differential electroresponsiveness of stellate and pyramidal-like cells of medial entorhinal cortex layer II. J. Neurophysiol. *70*, 128–143.

Amaral, D.G., and Witter, M.P. (1989). The three-dimensional organization of the hippocampal formation: a review of anatomical data. Neuroscience *31*, 571–591.

Barnes-Davies, M., Barker, M.C., Osmani, F., and Forsythe, I.D. (2004). Kv1 currents mediate a gradient of principal neuron excitability across the tonotopic axis in the rat lateral superior olive. Eur. J. Neurosci. *19*, 325–333.

BoSmith, R.E., Briggs, I., and Sturgess, N.C. (1993). Inhibitory actions of ZENECA ZD7288 on whole-cell hyperpolarization activated inward current (If) in guinea-pig dissociated sinoatrial node cells. Br. J. Pharmacol. *110*, 343–349.

Brun, V.H., Solstad, T., Kjelstrup, K.B., Fyhn, M., Witter, M.P., Moser, E.I., and Moser, M.-B. (2008). Progressive increase in grid scale from dorsal to ventral medial entorhinal cortex. Hippocampus *18*, 1200–1212.

Buckmaster, P.S., Alonso, A., Canfield, D.R., and Amaral, D.G. (2004). Dendritic morphology, local circuitry, and intrinsic electrophysiology of principal neurons in the entorhinal cortex of macaque monkeys. J. Comp. Neurol. *470*, 317–329.

Burgess, N., Barry, C., and O'Keefe, J. (2007). An oscillatory interference model of grid cell firing. Hippocampus *17*, 801–812.

Burwell, R.D. (2000). The parahippocampal region: corticocortical connectivity. Ann. N Y Acad. Sci. *911*, 25–42.

Buzsaki, G. (2002). Theta oscillations in the hippocampus. Neuron *33*, 325–340.

Carnevale, N.T., and Hines, M.L. (2006). The NEURON book (Cambridge: Cambridge University Press).

Chrobak, J.J., and Buzsaki, G. (1998). Gamma oscillations in the entorhinal cortex of the freely behaving rat. J. Neurosci. *18*, 388–398.

Coetzee, W.A., Amarillo, Y., Chiu, J., Chow, A., Lau, D., McCormack, T., Moreno, H., Nadal, M.S., Ozaita, A., Pountney, D., et al. (1999). Molecular diversity of K+ channels. Ann. N Y Acad. Sci. *868*, 233–285.

Dan, Y., and Poo, M.M. (2004). Spike timing-dependent plasticity of neural circuits. Neuron *44*, 23–30.

Dickson, C.T., Magistretti, J., Shalinsky, M.H., Fransen, E., Hasselmo, M.E., and Alonso, A. (2000). Properties and role of I(h) in the pacing of subthreshold oscillations in entorhinal cortex layer II neurons. J. Neurophysiol. *83*, 2562–2579.

Dolorfo, C.L., and Amaral, D.G. (1998). Entorhinal cortex of the rat: topographic organization of the cells of origin of the perforant path projection to the dentate gyrus. J. Comp. Neurol. *398*, 25–48.

Fyhn, M., Hafting, T., Witter, M.P., Moser, E.I., and Moser, M.B. (2008). Grid cells in mice. Hippocampus, in press. Published online August 6, 2008. 10.1002/hipo.20472.

Giocomo, L.M., and Hasselmo, M.E. (2008). Time constants of h current in layer ii stellate cells differ along the dorsal to ventral axis of medial entorhinal cortex. J. Neurosci. *28*, 9414–9425.

Giocomo, L.M., Zilli, E.A., Fransen, E., and Hasselmo, M.E. (2007). Temporal frequency of subthreshold oscillations scales with entorhinal grid cell field spacing. Science *315*, 1719–1722.

Goldstein, S.A., Bockenhauer, D., O'Kelly, I., and Zilberberg, N. (2001). Potassium leak channels and the KCNK family of two-P-domain subunits. Nat. Rev. Neurosci. *2*, 175–184.

Goldstein, S.A., Bayliss, D.A., Kim, D., Lesage, F., Plant, L.D., and Rajan, S. (2005). International Union of Pharmacology. LV. Nomenclature and molecular relationships of two-P potassium channels. Pharmacol. Rev. *57*, 527–540.

Hafting, T., Fyhn, M., Molden, S., Moser, M.B., and Moser, E.I. (2005). Microstructure of a spatial map in the entorhinal cortex. Nature *436*, 801–806.

Hafting, T., Fyhn, M., Bonnevie, T., Moser, M.B., and Moser, E.I. (2008). Hippocampus-independent phase precession in entorhinal grid cells. Nature *453*, 1248–1252.

Hattox, A.M., and Nelson, S.B. (2007). Layer v neurons in mouse cortex projecting to different targets have distinct physiological properties. J. Neurophysiol. *98*, 3330–3340.

Hausser, M., and Roth, A. (1997). Estimating the time course of the excitatory synaptic conductance in neocortical pyramidal cells using a novel voltage jump method. J. Neurosci. *17*, 7606–7625.

Hausser, M., Spruston, N., and Stuart, G.J. (2000). Diversity and dynamics of dendritic signaling. Science *290*, 739–744.

Hopfield, J.J. (1982). Neural networks and physical systems with emergent collective computational abilities. Proc. Natl. Acad. Sci. USA *79*, 2554–2558.

Jack, J.J.B., Noble, D., and Tsien, R.W. (1975). Electric current flow in excitable cells (Oxford: Clarendon Press).

Klink, R., and Alonso, A. (1997). Morphological characteristics of layer II projection neurons in the rat medial entorhinal cortex. Hippocampus *7*, 571–583.

Koch, C. (1999). Biophysics of computation: information processing in single neurons (New York: Oxford University Press).

Kubo, Y., Adelman, J.P., Clapham, D.E., Jan, L.Y., Karschin, A., Kurachi, Y., Lazdunski, M., Nichols, C.G., Seino, S., and Vandenberg, C.A. (2005). International Union of Pharmacology. LIV. Nomenclature and molecular relationships of inwardly rectifying potassium channels. Pharmacol. Rev. *57*, 509–526.

Kumar, S.S., Jin, X., Buckmaster, P.S., and Huguenard, J.R. (2007). Recurrent circuits in layer II of medial entorhinal cortex in a model of temporal lobe epilepsy. J. Neurosci. *27*, 1239–1246.

Laughlin, S. (1981). A simple coding procedure enhances a neuron's information capacity. Z Naturforsch [C] *36*, 910–912.

Lein, E.S., Hawrylycz, M.J., Ao, N., Ayres, M., Bensinger, A., Bernard, A., Boe, A.F., Boguski, M.S., Brockway, K.S., Byrnes, E.J., et al. (2007). Genome-wide atlas of gene expression in the adult mouse brain. Nature *445*, 168–176.

Magee, J.C. (2000). Dendritic integration of excitatory synaptic input. Nat. Rev. Neurosci. *1*, 181–190.

Markram, H., Toledo-Rodriguez, M., Wang, Y., Gupta, A., Silberberg, G., and Wu, C. (2004). Interneurons of the neocortical inhibitory system. Nat. Rev. Neurosci. *5*, 793–807.

McCormick, D.A., Connors, B.W., Lighthall, J.W., and Prince, D.A. (1985). Comparative electrophysiology of pyramidal and sparsely spiny stellate neurons of the neocortex. J. Neurophysiol. *54*, 782–806.

McLean, D.L., Fan, J., Higashijima, S., Hale, M.E., and Fetcho, J.R. (2007). A topographic map of recruitment in spinal cord. Nature *446*, 71–75.

Moser, E.I., Kropff, E., and Moser, M.B. (2008). Place cells, grid cells, and the brain's spatial representation system. Annu. Rev. Neurosci. *31*, 69–89.

Nolan, M.F., Dudman, J.T., Dodson, P.D., and Santoro, B. (2007). HCN1 channels control resting and active integrative properties of stellate cells from layer II of the entorhinal cortex. J. Neurosci. *27*, 12440–12451.

Rall, W. (1960). Membrane potential transients and membrane time constant of motoneurons. Exp. Neurol. *2*, 503–532.

Reid, M.A., Flores-Otero, J., and Davis, R.L. (2004). Firing patterns of type II spiral ganglion neurons in vitro. J. Neurosci. *24*, 733–742.

Robinson, R.B., and Siegelbaum, S.A. (2003). Hyperpolarization-activated cation currents: from molecules to physiological function. Annu. Rev. Physiol. *65*, 453–480.

Spruston, N., and Johnston, D. (1992). Perforated patch-clamp analysis of the passive membrane properties of three classes of hippocampal neurons. J. Neurophysiol. *67*, 508–529.

Steffenach, H.A., Witter, M., Moser, M.B., and Moser, E.I. (2005). Spatial memory in the rat requires the dorsolateral band of the entorhinal cortex. Neuron *45*, 301–313.

Stemmler, M., and Koch, C. (1999). How voltage-dependent conductances can adapt to maximize the information encoded by neuronal firing rate. Nat. Neurosci. *2*, 521–527.

Sugino, K., Hempel, C.M., Miller, M.N., Hattox, A.M., Shapiro, P., Wu, C., Huang, Z.J., and Nelson, S.B. (2006). Molecular taxonomy of major neuronal classes in the adult mouse forebrain. Nat. Neurosci. *9*, 99–107.

van Groen, T., Miettinen, P., and Kadish, I. (2003). The entorhinal cortex of the mouse: organization of the projection to the hippocampal formation. Hippocampus *13*, 133–149.

Wang, X.J. (2001). Synaptic reverberation underlying mnemonic persistent activity. Trends Neurosci. *24*, 455–463.

Williams, S.R., and Stuart, G.J. (2003). Role of dendritic synapse location in the control of action potential output. Trends Neurosci. *26*, 147–154.

Williams, S.R., and Mitchell, S.J. (2008). Direct measurement of somatic voltage clamp errors in central neurons. Nat. Neurosci. *11*, 790–798.

Witter, M.P., Wouterlood, F.G., Naber, P.A., and Van Haeften, T. (2000). Anatomical organization of the parahippocampal-hippocampal network. Ann. N Y Acad. Sci. *911*, 1–24.

Yuste, R. (2005). Origin and classification of neocortical interneurons. Neuron *48*, 524–527.